Author's personal copy

Available online at www.sciencedirect.com
ScienceDirect
Acta Materialia 59 (2011) 3484–3497
Acta MATERIALIA
www.elsevier.com/locate/actamat

Modeling displacive–diffusional coupled dislocation shearing of γ′ precipitates in Ni-base superalloys

Ning Zhou [a], Chen Shen [b], Michael J. Mills [a], Ju Li [c], Yunzhi Wang [a,*]

[a] Department of Materials Science and Engineering, The Ohio State University, 2041 College Road, Columbus, OH 43210, USA
[b] GE Global Research, 1 Research Circle, Niskayuna, NY 12309, USA
[c] Department of Materials Science and Engineering, University of Pennsylvania, 223 LRSM, 3231 Walnut Street, Philadelphia, PA 19104, USA

Received 21 January 2011; received in revised form 7 February 2011; accepted 14 February 2011
Available online 21 March 2011

Abstract

In Ni-base superalloys, superlattice extrinsic stacking fault (SESF) shearing of γ′ precipitates involves coupled dislocation glide and atomic diffusion. A phase-field model is developed to study this process, in which the free energy of the system is formulated as a function of both displacement and long-range order parameter. The free energy surface is fitted to various fault energy data obtained from experiments and *ab initio* calculations. Three-dimensional simulations at experimentally relevant length scales are carried out to investigate systematically the influence of microstructural features on the critical resolved shear stress. The simulations reveal that the critical resolved shear stress for SESF shearing is determined not only by the SESF energy itself, but also by the complex stacking fault energy and by the shape (interface curvature) and spacing of γ′ precipitates. The effect of reordering kinetics (i.e. temperature effect) is also investigated. It is found that viscous deformation can only occur within certain domain of intermediate temperatures.
© 2011 Acta Materialia Inc. Published by Elsevier Ltd. All rights reserved.

Keywords: Plasticity; Deformation twinning; Diffusion; Atomic ordering; Phase field

1. Introduction

Plastic deformation and microstructural evolution in crystalline solids are often controlled by mechanochemical or displacive–diffusional coupled processes. Consider, for instance, dislocation–precipitate interactions in Ni-base superalloys. Dislocation shearing processes can couple strongly to diffusive processes such as chemical reordering in governing the rate of deformation (see Ref. [1] for a recent review). On the other hand, dislocation plasticity can also change the precipitate microstructure in a so-called directional coarsening or rafting process [2–4]. While extensive efforts have recently been made to simulate coupled γ′ microstructural evolution and γ-channel dislocation plasticity during rafting of high misfit superalloys for turbine blade applications [5–11], limited work has been done on the diffusion-mediated shearing process of γ′ particles in low-misfit superalloys for turbine disk applications. Although disk alloys are not, like turbine blades, projecting directly into the hot gas stream, they work under much higher stress (up to 1000 MPa) at intermediate temperatures (around 650 °C) [12]. Thus they exhibit even more complicated deformation behaviors [13–15] as compared to the blade alloys. As discovered recently through experimental characterization [1,16], superlattice extrinsic stacking fault (SESF) shearing is one of the important deformation mechanisms occurring in Ni-base superalloys under such service conditions.

Depending on temperature and stress, the interactions between dislocations and γ′ particles may follow several distinct paths. The typical microstructure of a disk alloy (such as Rene88 or Rene104) contains fully coherent secondary and tertiary γ′ particles (Ni_3Al with $L1_2$ structure) in the γ matrix (Ni based face-centered cubic (fcc) solid solution) [17]. At low temperatures (<600 °C), the deformation

* Corresponding author. Tel.: +1 614 292 0682; fax: +1 614 292 1537.
E-mail address: wang.363@osu.edu (Y. Wang).

1359-6454/$36.00 © 2011 Acta Materialia Inc. Published by Elsevier Ltd. All rights reserved.
doi:10.1016/j.actamat.2011.02.022

Author's personal copy

mechanism is dominated by shearing of γ' via paired a/$2\langle 1\,1\,0\rangle$ type dislocations with an anti-phase-boundary (APB) in between [18–20]. However, at much higher temperatures (>800 °C), climb of individual a/$2\langle 1\,1\,0\rangle$ dislocations bypassing γ' particles becomes the dominant deformation mechanism [2,21]. At temperatures between 600 and 800 °C, multiple deformation mechanisms have been reported, such as formation of isolated faults by SESF or superlattice intrinsic stacking fault (SISF) shearing [22–25], formation of stacking fault ribbon [26–28], and formation of extended faults that traverse the matrix and precipitates [13,22,29]. A typical deformation mechanism that demonstrates viscous behavior was proposed by Kolbe [30]. As two identical a/$6\langle 1\,1\,2\rangle$ Shockley partials shearing on adjacent {1 1 1} planes, thermal activation is required for atomic reordering to form SESFs in the γ' phase. Thus, it links the temperature effect directly to plastic deformation by showing the critical role played by short-range diffusion (atomic ordering) during creep test at intermediate temperatures. This mechanism leaves thin twin plates (around 4–50 atomic layers thick) propagating through both precipitates (via SESF shearing of the γ' particles) and γ matrix, which is often referred to as "microtwinning".

The objective of this paper is to study the diffusion-mediated SESF shearing process via computer simulations using the phase-field method. Other deformation mechanisms that might involve reordering include "isolated" SESF, SISF shearing by a/3[1 1 2] dislocations and stacking fault ribbons operated by a[1 1 2] dislocations [1]. In order to study these diffusion-mediated shearing processes, we introduce a long-range order parameter and ordering kinetics [31] into the microscopic phase-field model of dislocations [32–34] to describe the reordering process that leads to the formation of microtwins. The free energy of the system is formulated as a function of both displacement and long-range order parameter fields. Ab initio calculations and experimental data on various fault energies are utilized in the free energy formulation. Computer simulations and analytical calculations are carried out to investigate how microstructural and materials parameters such as size, shape and spatial distribution of γ' particles, precipitate–matrix interfacial width, reordering kinetics (temperature) and various fault energies influence the SESF shearing process.

In the following section, the generalized stacking fault (GSF) energy landscapes of the ordered and disordered phases and the SESF shearing process are presented, together with the introduction of a free energy surface formulated for the shear–diffusion coupling. The formulation of the elastic energy and the kinetic equations are also presented in Section 2. Simulation results of SESF shearing under different stress levels and reordering kinetics are presented in Section 3. Discussions on how microstructure features such as γ' particle size, shape and material parameters such as complex stacking fault (CSF) energy and γ–γ' interface width affect the critical resolved shear stress (CRSS) for SESF shearing are included in Section 4.

2. Model formulation

2.1. Generalized stacking fault energy surface and minimum energy pathway

The GSF energy surface (also referred to as the "Γ-surface") characterizes the potential energy landscape with respect to an arbitrary displacement on a given glide plane [35]. In both the γ (fcc solid solution) and γ' ($L1_2$) phases in Ni-base superalloys, the {1 1 1} octahedral planes are the common slip planes and the GSF energy landscape of the {1 1 1} slip plane defines the minimum energy path (MEP) of a specific shearing process. Such GSF energy contours for both the γ and γ' phases in a binary Ni–Al alloy determined by *ab initio* calculations [1,33,34] are shown in Fig. 1. All faults are indicated on the Γ-surface by different symbols. The focus of this study is on the shearing along one of the $\langle 1\,1\,2\rangle$ directions, which is the x-axis on the plot. The solid arrows and dotted arrows represent the shearing mode of the a/$6\langle 1\,1\,2\rangle$ type partial dislocations, which first creates an intrinsic stacking fault (ISF) in the γ matrix. The ISF then changes to an extrinsic stacking fault (ESF) after the second partial (with the same Burgers vector but one atomic layer above the slip plane of the first one) shears through. While in the γ' phase, the same process creates first a CSF and then a two-layer pseudo-twin structure. Both the CSF and the pseudo-twin structure are high-energy configurations that prevent further shearing of γ'. However, if atomic reordering could take place, the pseudo-twin structure will be converted into a true twin structure via the formation of the low-energy SESF. Thus, the additional structural reordering degree of freedom cannot be overlooked when constructing the free energy landscape to identify the minimum energy pathway for the shearing deformation process of γ' phase at elevated temperatures.

Since the shearing mode of interest in the above process is along a single direction, i.e. the $\langle 1\,1\,2\rangle$ direction, the GSF energy landscape of both phases along this direction has been determined using *ab initio* calculations [33]. The result, $\Gamma_{st}(\eta)$, is shown by the thick solid line (black) in Fig. 2, where the x-axis (η) represents the magnitude of the $\langle 1\,1\,2\rangle$ displacement vector in reduced unit $\eta \equiv u/\left(\sqrt{6}a/6\right)$, where a is the lattice constant, u is the displacement) and y-axis (f) is the stacking fault energy (in mJ m^{-2}). The dotted yellow[1] curve $\Gamma_{\gamma}(\eta)$ represents the GSF energy landscape along $\langle 1\,1\,2\rangle$ in the γ phase. It is readily seen that the energy of the pseudo-twin configuration is extremely high (about twice the CSF energy). In order to explore the minimum energy path of the deformation when atomic reordering is allowed, a long-range order (lro) parameter, ϕ, is introduced to characterize the degree of reordering [31,36]. The introduction of ϕ forms a new

[1] For interpretation of color in Figs. 1–4, 10, 13 and 15, the reader is referred to the web version of this article.

Author's personal copy

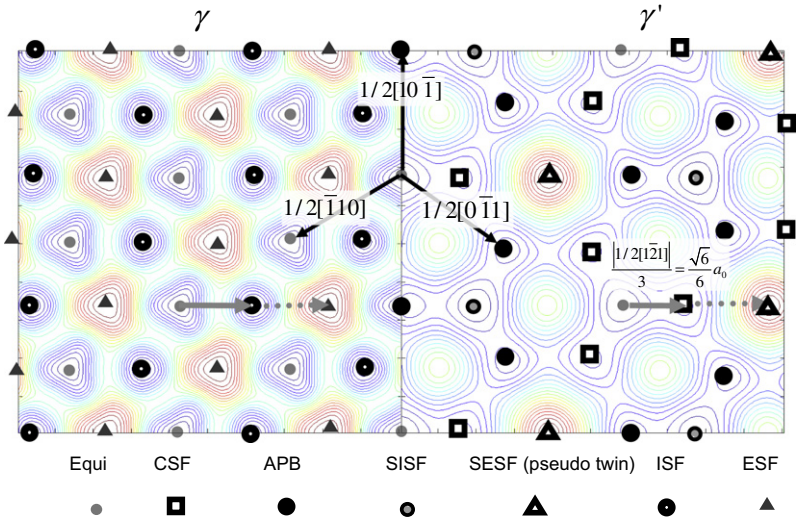

Fig. 1. Γ-surface of γ and γ′ phase for {1 1 1} slip plane.

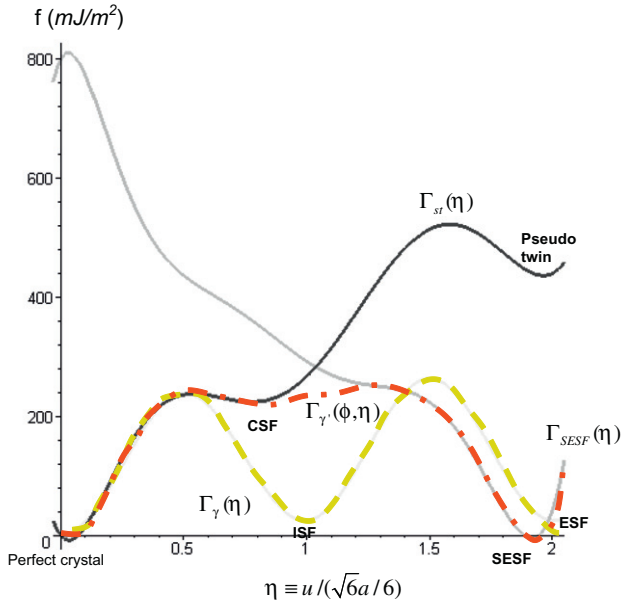

Fig. 2. Energy contour projection along the ⟨1 1 2⟩ shearing direction.

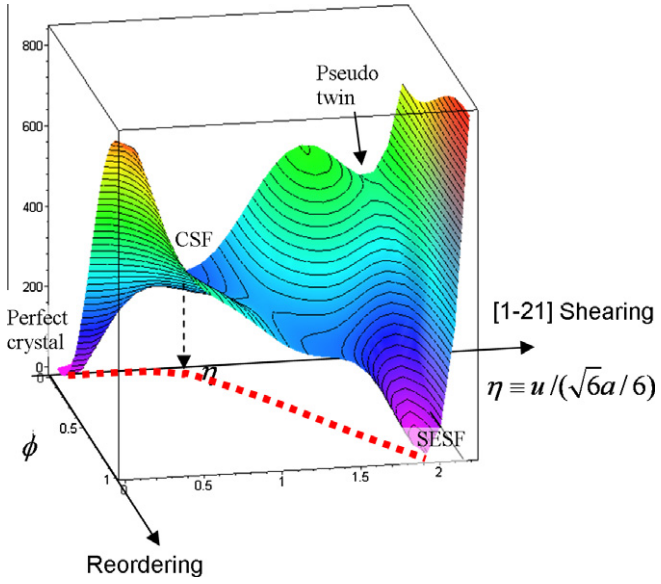

Fig. 3. 2-D energy surface for γ′ phase $\Gamma_{\gamma'}(\phi,\eta)$.

degree of freedom of the GSF energy landscape and a new GSF energy surface in the $\eta-\phi$ space is created, as shown in Fig. 3. When reordering is prohibited, $\phi=0$ and the system follows the thick solid (black) curve shown in Fig. 2. When reordering is allowed, the system will follow the MEP defined by this new GSF energy surface, which leads to the formation of an SESF rather than a pseudo-twin. Because of the lack of both experimental data and *ab initio* calculations, the GSF energy surface show in Fig. 3 is constructed in a phenomenological way by fitting the surface to the $\Gamma_{st}(\eta)$ curve show in Fig. 2 obtained by *ab initio* calculations [1,33] and SESF energy estimation from experimental measurement [37], i.e.

$$\Gamma_{\gamma'}(\phi,\eta)=(1-P(\phi))\cdot\Gamma_{st}(\eta)+P(\phi)\cdot\Gamma_{SESF}(\eta) \tag{1}$$

where

$$\begin{aligned}\Gamma_{st}(\eta)&=7.474\times10^{-4}-5.087\times10^{2}\eta+8.612\times10^{3}\eta^{2}\\&\quad-2.452\times10^{4}\eta^{3}+3.065\times10^{4}\eta^{4}-1.926\\&\quad\times10^{4}\eta^{5}+6.163\times10^{3}\eta^{6}-9.17\times10^{2}\eta^{7}\\&\quad+4.672\times10^{1}\eta^{8}(\mathrm{mJ/m^2})\end{aligned} \tag{2}$$

$$\begin{aligned}\Gamma_{SESF}(\eta)&=8.000\times10^{2}+7.655\times10^{2}\eta-1.431\\&\quad\times10^{4}\eta^{2}+4.798\times10^{4}\eta^{3}-7.751\times10^{4}\eta^{4}\\&\quad+6.852\times10^{4}\eta^{5}-3.357\times10^{4}\eta^{6}+8.482\\&\quad\times10^{3}\eta^{7}-8.522\times10^{2}\eta^{8}\quad(\mathrm{mJ/m^2})\end{aligned} \tag{3}$$

and

$$P(\phi)=(\phi)^{3}(10-15\phi+6(\phi)^{2}) \tag{4}$$

Author's personal copy

$\Gamma_{SESF}(\eta)$ is plotted as a gray solid line in Fig. 2. When atomistic calculations become available, $\Gamma_{SESF}(\eta)$ should be replaced by *ab initio* data and the entire surface, $\Gamma_{\gamma\prime}(\phi,\eta)$, could be constructed by either kinetic Monte Carlo [38] or temperature-accelerated molecular dynamics simulations [39]. For the current study, the GSF energy surface shown in Fig. 3 and the MEP along the reaction coordinate defined in the $\eta-\phi$ space (the projection of the MEP on $\eta-\phi$ plane) indicated by the dashed line can only be regarded as qualitative.

The 1-D projection of $\Gamma_{\gamma\prime}(\phi,\eta)$ along the MEP from perfect crystal to CSF and to SESF is indicated by the dot-dash (red) line in Fig. 2 for cases with instantaneous atomic reordering. The real path depends on the magnitude of the resolved shear stress and the kinetics of the reordering process. The CSF energy used for the fitting is $\Gamma^{CSF}=221$ mJ/m^2 [33] and the SESF energy is $\Gamma^{SESF}=25$ mJ/m^2, which is set equal to the ISF energy [40].

The crystalline energy in the phase-field model [41] at a specific position $\mathbf{r}$ in the system is obtained by introducing a shape function, $\theta(\mathbf{r})$. This parameter dictates which phase (γ or γ') is located at $\mathbf{r}$: $\theta=0$ for the γ phase and $\theta=1$ for the γ' phase. The crystalline energy for a $\gamma+\gamma'$ two-phase mixture as a function of the displacement field η and the lro parameter field ϕ is then obtained by linking the GSF energy functions of the individual γ and γ' phases through an interpolation function:

$$E^{crystal}(\theta,\phi,\eta)=(1-P(\theta))\cdot\Gamma_{\gamma}(\eta)+P(\theta)\cdot\Gamma_{\gamma\prime}(\phi,\eta) \tag{5}$$

$$P(\theta)=(\theta)^3(10-15\theta+6(\theta)^2) \tag{6}$$

where $\Gamma_{\gamma}(\eta)$ is the GSF energy of the γ phase which is approximated by a simple combination of sinusoidal functions fitted to the intrinsic and extrinsic stacking fault energies for computational efficiency:

$$\Gamma_{\gamma}(\eta)=1.150\times10^2\{\sin[\pi(2\eta-0.5)]+1.0\}+1.667\times10\left\{\sin\left[\frac{\pi(\eta-0.75)}{1.5}\right]+1.0\right\}\quad(\mathrm{mJ/m^2}) \tag{7}$$

This gives 25 mJ m^{-2} for the ISF energy at $\eta=1$, and 25 mJ m^{-2} for the ESF energy at $\eta=2$, as illustrated by the yellow dotted curve in Fig. 2. The shape function $\theta(\mathbf{r})$ will not be evolved in this study as the coarsening of the γ/γ' microstructure is a much slower process as compared to the shearing processes, and the atomic steps on the surface of the γ' particles created by the shearing processes cannot be resolved in such mesoscale simulations.

The construction of such an energy landscape shown in Fig. 3 extends the concept of GSF energy from a function of pure displacive degree of freedom to a more general formulation that takes into account the diffusional degrees of freedom during a deformation process. It should be noted that displacive–diffusional coupling during deformation is a general phenomenon rather than an exception [42]. Well-known examples of diffusion-aided deformation include Nabarro–Herring [43,44] and Coble [45] creep, power-law creep involving dislocation climb [46], Asaro–Tiller–Grinfeld instability [47,48], and solute drag on dislocations [49], to name a few.

2.2. Elastic strain energy

In the phase-field model, the elastic strain energy (including the work term done by an external load) of a system having an arbitrary dislocation configuration is calculated based on Khachaturyan and Shotalov's microelasticity theory [50–52]:

$$E^{elastic}(\theta,\eta)=\frac{1}{2}\int\frac{d\mathbf{k}}{(2\pi)^3}\left[C_{ijkl}\tilde{\varepsilon}^T_{ij}(\mathbf{k})\tilde{\varepsilon}^{T*}_{kl}(\mathbf{k})-n_i\tilde{\sigma}^T_{ij}(\mathbf{k})\Omega_{jk}(\mathbf{n})\tilde{\sigma}^{T*}_{kl}(\mathbf{k})n_l\right]-\int d\mathbf{r}\left[\sigma^{app}_{ij}\varepsilon^T_{ij}(\mathbf{r})\right] \tag{8}$$

where C_{ijkl} is the stiffness tensor, $\mathbf{n}$ is a unit vector in $\mathbf{k}$-space, the superscript asterisk denotes the complex conjugate, $\Omega_{ij}(\mathbf{n})$ is the Green function tensor inverse to $\Omega^{-1}_{ij}(\mathbf{n})=C_{iklj}n_kn_l$, and $\varepsilon^T_{ij}(\mathbf{r})$ is the stress-free transformation strain (SFTS) field and its Fourier transform $\tilde{\varepsilon}^T_{ij}(\mathbf{k})=\int_V\varepsilon^T_{ij}(\mathbf{r})e^{-i\mathbf{k}\cdot\mathbf{r}}d\mathrm{r}$, $\sigma^T_{ij}(\mathbf{r})=C_{ijkl}\varepsilon^T_{kl}(\mathbf{r})$ and its Fourier transform $\tilde{\sigma}^T_{ij}(\mathbf{k})=\int_V\sigma^T_{ij}(\mathbf{r})e^{-i\mathbf{k}\cdot\mathbf{r}}d\mathbf{r}$, σ^{app}_{ij} is an externally applied stress. The first part of integration excludes a volume $(2\pi)^3/V$ around the point $\mathbf{k}=0$.

The SFTS field in an arbitrary microstructure consisting of coherent precipitates and dislocations can be formulated as [5,6,8,9,41]:

$$\varepsilon^T_{ij}(\mathbf{r})=\delta_{ij}\frac{2(a_{\gamma\prime}-a_{\gamma})}{(a_{\gamma\prime}+a_{\gamma})}\theta(\mathbf{r})+\sum_{\alpha=1\ldots p}\frac{b^{\alpha}_im^{\alpha}_j+m^{\alpha}_ib^{\alpha}_j}{2d}\eta(\mathbf{r}) \tag{9}$$

where δ_{ij} is the Kronecker delta, $a_{\gamma\prime}$ and a_{γ} are the lattice parameters of the γ' and γ phases, respectively, p is the number of slip systems, $\mathbf{m}^{\alpha}$ is the slip plane normal for slip system α and $\mathbf{b}^{\alpha}$ denotes its Burgers vector, and d is the interplanar spacing of the slip plane. The first term of this SFTS formula describes the lattice mismatch between the γ and γ' phases, which is close to zero in most Ni-base disk alloys. Thus, only the second term, the eigenstrain of dislocations, is considered in this study.

2.3. Total energy

The total energy of the system E is a sum of the crystalline energy, the elastic strain energy and the gradient energy, i.e.:

$$E=\int d^3r[E^{crystal}(\theta,\phi,\eta)/d_{(111)}+f^{grad}(\nabla\eta)]+E^{elastic}(\theta,\eta) \tag{10}$$

where $f^{grad}(\nabla\eta)$ is the gradient energy of the displacement field, which is related to the dislocation core energy [32,34,41,53] and is required for coarse-graining.

2.4. Kinetic equations

The minimization of the total energy E with respect to both the lro parameter ϕ and the inelastic strain field (i.e.

Author's personal copy

the displacement field η) is carried out numerically by solving the time-dependent Ginzburg–Landau equations:

$$\frac{\partial \phi}{\partial t} = -L\frac{\delta E}{\delta \phi} \tag{11}$$

$$\frac{\partial \eta}{\partial t} = -M_\eta \frac{\delta E}{\delta \eta} \tag{12}$$

where L is the kinetic coefficient for atomic ordering and M_η is the dislocation mobility.

2.5. Coarse-graining

Phase-field models, when applied at nanometer length scales, i.e. at a resolution comparable to the cores of extended defects (usually called microscopic phase-field models) [32,34], can make quantitative predictions of fundamental properties of individual defects (e.g. size, formation energy, saddle-point configuration and activation energy of defect nuclei, and the micromechanisms of their mutual interactions). However, extending these models to a typical γ/γ' microstructure in Ni-base superalloy requires proper coarse-graining. Because of the diffuse interface nature of the phase-field method, the boundary or core energy will be unrealistically large when the simulation grid size is at the mesoscale. As will be seen in Sections 3 and 4, the line-tension of dislocations, the local curvature of γ/γ' interfaces and the γ-channel width all play critical roles in determining the critical stress for SESF shearing. Therefore, it is important for the phase-field model to capture the correct line tension and interfacial energy at the relevant length scales (such as the scanning electron microscopy image shown in Fig. 5a).

Methods have been developed for treating precipitates at coarse-grained length scales [36,54–57] without encountering unrealistically high interfacial energy. These approaches, however, do not apply to the non-conserved displacement fields introduced in phase-field dislocation models where a single continuous GSF energy with respect to the displacement vector is used. As the GSF energy contains crucial information, such as different fault energies and shear modulus, a new way of coarse-graining has been developed without altering the GSF energy. This so-called "curvature correction" method compensates the exaggerated dislocation line tension by exerting additional stress on the dislocation line with its magnitude adjusted according to the length scale and the dislocation local curvature: $\tau(\mathbf{x}) = (\beta - 1)\frac{\mu b^2 V_m \rho(\mathbf{x})}{2d}$, where β is the scaling factor depending on the length scale (how many times the dislocation line tension is exaggerated, i.e. $T = \beta\frac{\mu b^2}{2}$), μ is the shear modulus, b is the Burgers vector, V_m is the molar volume and d is the spacing between neighboring slip planes. The local curvature $\rho(\mathbf{x})$ of the dislocation line can be easily obtained based on the field description of the displacement field [58]. The detailed formulation of this method will be presented in a forthcoming paper [59]. In this study we have adopted this new approach to obtain the correct interfacial energy and dislocation line tension at micrometer length scales.

3. Simulation results

3.1. Curvature correction of dislocation line tension

Using the rescaling method based on local curvature correction mentioned above, the exaggerated curvature effect at the mesoscale in a coarse-grained phase-field model can be corrected by keeping track of the local curvature of the phase-field boundary and modifying its energy. Thus the artifact of exaggerated dislocation line tension in the mesoscale phase-field simulation can be avoided. Benchmark tests are performed to obtain the critical stress needed to stabilize a partial dislocation loop (with ISF inside or outside the loop). As shown in Fig. 4, before implementing the correction the critical stress turns out to be much higher, which corresponds to a line tension of $T = 2.9\frac{\mu b^2}{2}$ (filled triangles). However, after the curvature correction (filled squares), the critical stress is restored to match the analytical results for a line tension of $T = \frac{\mu b^2}{2}$.

3.2. System size, material parameters and initial conditions

The material parameters used in the simulation are listed in Table 1. The system size for the numerical simulations is $512 \times 512 \times 512$, with a grid size of $l_0 = 1.95$ nm. The (1 1 1) slip plane is orientated to coincide with one of the x–y planes of the simulation cell. The γ/γ' microstructure (assuming it is a $\{1\,1\,1\}$ cross-section which corresponds to one of the octahedral slip planes) is shown in Fig. 5, where the energy-filtered TEM (EFTEM) image using the $L_{2,3}$ Cr edge [60] in Fig. 5a [17] is digitized and used in the phase-field simulations (Fig. 5b). In this EFTEM image, the γ' particles appear dark since Cr strongly partitions to the γ matrix. In Fig. 5b, the γ' particles in the left region ($x < 100$ grids) are removed for the convenience of setting up the initial dislocation configuration (the region to the left of the dislocations is defined as sheared). The initial position of the leading $a/6\langle 1\,1\,2\rangle$ dislocation is indicated by the solid line, while the trailing one is indicated by the dashed line. This initial configuration will be used throughout all of the phase-field simulations.

3.3. Effect of curvature correction on dislocation kinetics

Fig. 6 shows the final equilibrium dislocation configuration under 500 MPa applied stress (without reordering) before implementing the curvature correction algorithm, where the dislocations failed to pass through the γ channels between γ' precipitates because of the high line tension. The contrast of the plot indicates local GSF energy where dislocation line and fault energy appear darker (higher energy). The interface of the γ/γ' phase is then superimposed onto the plot. For instance, the dislocation is represented as a thick black line, while ISFs/ESFs are

Author's personal copy

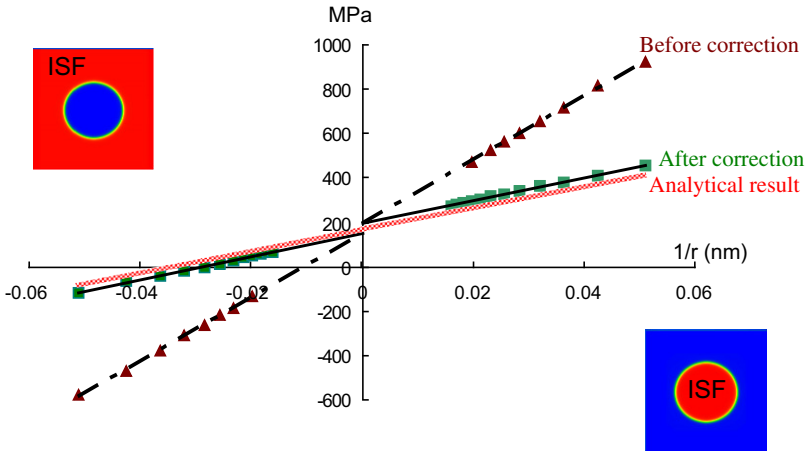

Fig. 4. Validation of curvature correction for a single partial dislocation loop (with intrinsic stacking fault). The triangular markers represent the stress needed to stabilize the partial dislocation loop as a function of the inverse of its radius before applying the curvature correction. The square markers represent the stress needed to stabilize the partial dislocation loop after applying the curvature correction. The shaded line is the analytical solution for the stress needed to stabilize the partial dislocation loop whose line tension is expressed as $T = \frac{\mu b^2}{2}$.

Table 1
Material parameters used for the simulation.

System size	1 μm × 1 μm × 1 μm (512 × 512 × 512)
Elastic moduli [61]	$C_{11} = 224.3$ GPa, $C_{12} = 148.6$ GPa, $C_{44} = 125.8$ GPa
Poisson's ratio	$v = 0.4$
Lattice constant	$a = 0.358$ nm
Burgers vector for partials	$b = a/6[1\bar{2}1]$
	$\|b\| = 0.146$ nm
Fault energies	$\Gamma^{ISF} = 25$ mJ/m^2 [40]; $\Gamma^{ESF} = 25$ mJ/m^2; $\Gamma^{SESF} = 25$ mJ/m^2; $\Gamma^{CSF} = 221$ mJ/m^2 [33]; $\Gamma^{\text{pseudo twin}} = 442$ mJ/m^2

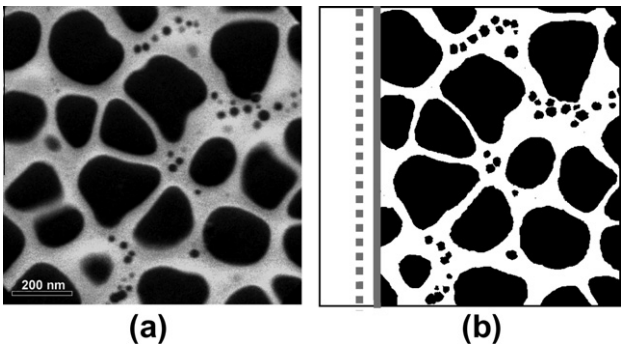

Fig. 5. (a) EFTEM image of γ–γ′ microstructure using the Cr $L_{2,3}$ edge and (b) digitized image with initial position of the leading (solid line) and trailing (dash line) dislocations.

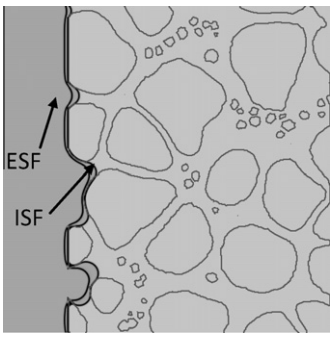

Fig. 6. Equilibrium dislocation configuration under 500 MPa shear stress (along $[1\bar{2}1]$, which is the Burgers vector direction for both dislocations) without curvature correction (e.g. dislocation line tension is $T = 2.9\frac{\mu b^2}{2}$). Reordering is not allowed.

represented by regions of darker shades of gray. After the curvature correction algorithm is implemented (Fig. 7a–c), the dislocations are able to pass through some of the γ channels under the same applied shear stress. Smaller particles are sheared by the first dislocation, leaving CSF (regions of black shade), while larger particles are looped around. The second dislocation is stopped before it can penetrate further because the γ-channel width is effectively reduced by the first partial that deposits segments along the γ/γ′ interface after it passes through (an example is indicated on Fig. 7b with a solid circle). Moreover, without reordering, a 500 MPa shear stress is not large enough for the second dislocation to shear through the small particles which will create the pseudo-twin structure (indicated on Fig. 7b with a dotted circle). Fig. 7d–f show the corresponding local curvature plot where the white color indicates positive curvature and the dark color negative curvature (with respect to the sheared region).

Author's personal copy

3.4. Effect of microstructure and reordering kinetics on SESF shearing

As shown in Fig. 7, in the absence of reordering, dislocations cannot shear through the γ' particles under 500 MPa resolved shear stress because of the high energy of the CSFs and pseudo-twins. Even if reordering is allowed (e.g. $L = 10$), however, dislocations still cannot shear through most of the γ' particles (Fig. 8). Only for those particles with sharp tips (as the position indicated by the arrow in Fig. 8a and b, which is caused by the periodic boundary condition) or small diameters (indicated by the arrow in Fig. 8c) can the SESF shearing mechanism operate.

If the applied stress is increased to 1000 MPa, for $L = 0$ (no reordering) (Fig. 9a–c), dislocations penetrate into most of the γ channels. Small γ' particles are sheared by the first dislocation, leading to CSF (regions of black shade) and then by the second dislocation, creating pseudo-twin (regions of gray shade).

If reordering is allowed, shearing of γ' precipitates will be influenced strongly by the reordering kinetics. To

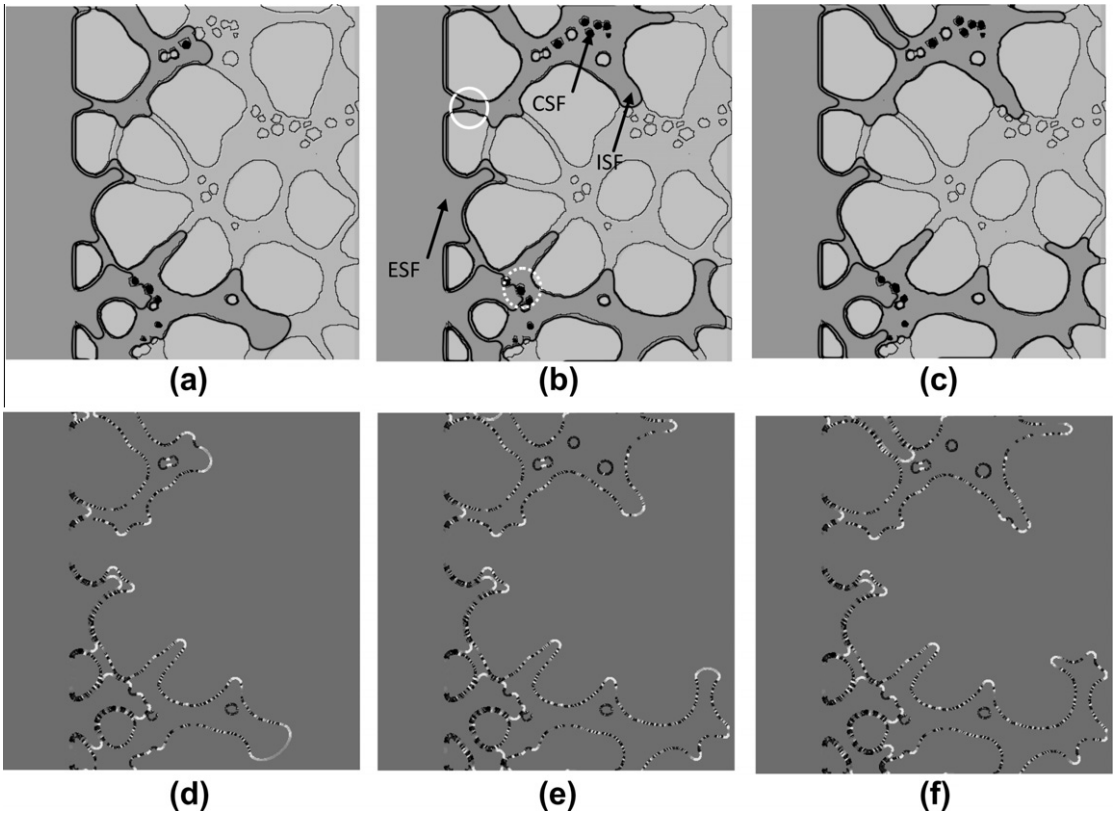

Fig. 7. (a–c) Dislocation configurations under 500 MPa shear stress (without reordering ($L = 0$) but with curvature correction) at reduced time $t^* = 33, 48, 64$; (d–f) the corresponding curvature plots (white color represents positive local curvature, black color represents negative curvature).

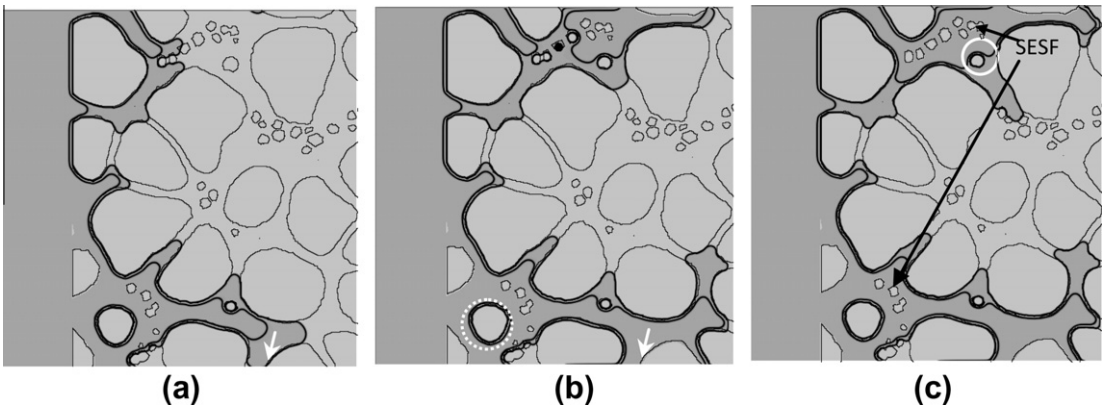

Fig. 8. Dislocation shearing of γ–γ' microstructure under 500 MPa resolved shear stress with reordering ($L = 10$). (a) $t^* = 3$, (b) $t^* = 10$, (c) $t^* = 18$, where t^* is a reduced time.

Author's personal copy

investigate this effect, a parametric study is carried out with different reordering mobility L under constant dislocation mobility. Fig. 9d–o shows the dislocation configurations for $L = 10$, 1 and 0.1 (in reduced units), respectively, at

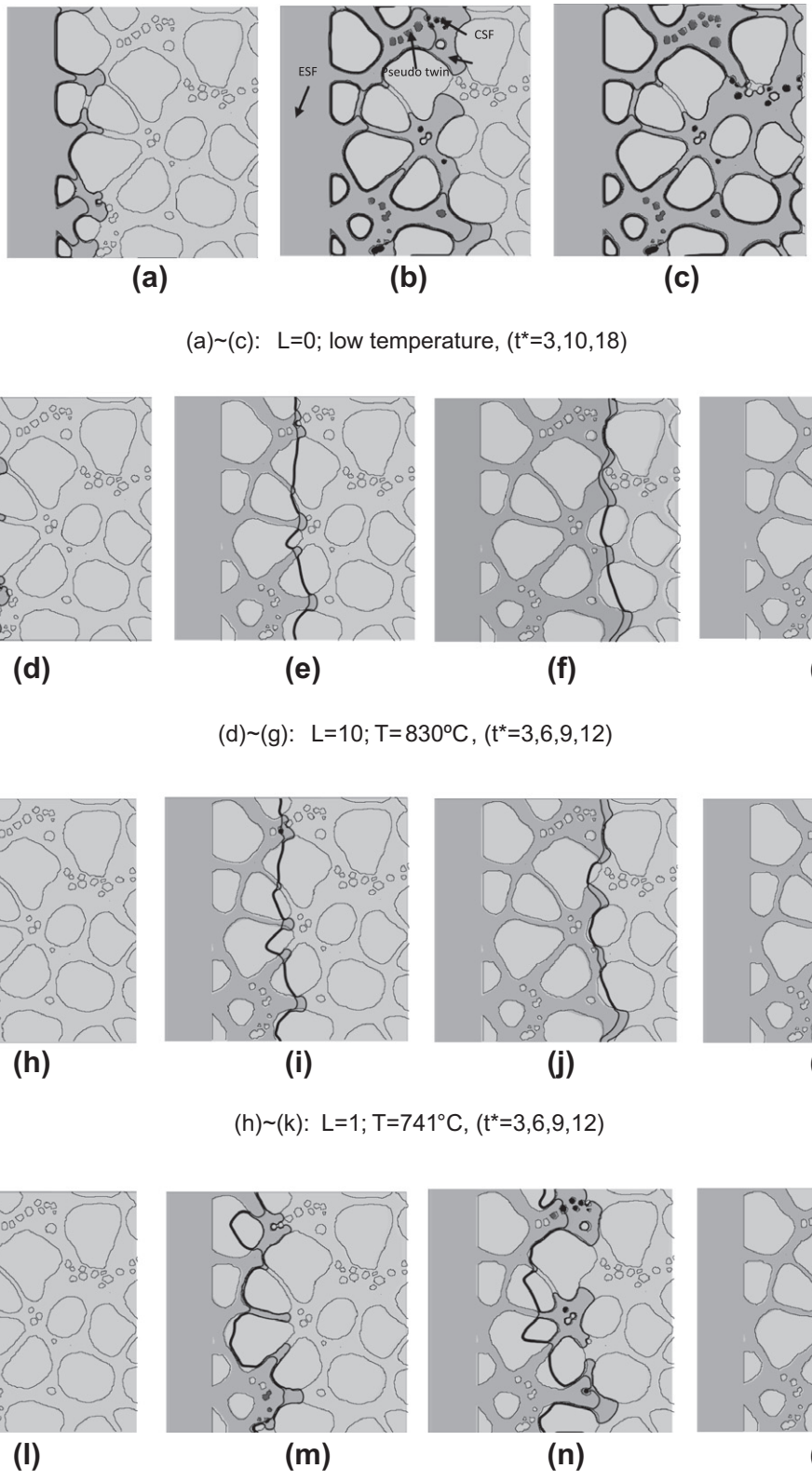

Fig. 9. Dislocation shearing of γ/γ' microstructure under 1000 MPa resolved shear stress with reordering. t^* is a reduced time. (a–c) $L = 0$; low temperature; (d–g) $L = 10$; $T = 830$ °C; (h–k) $L = 1$; $T = 741$ °C; (l–o) $L = 0.1$; $T = 665$ °C; (p–s) $L = 0.01$; $T = 600$ °C.

Author's personal copy

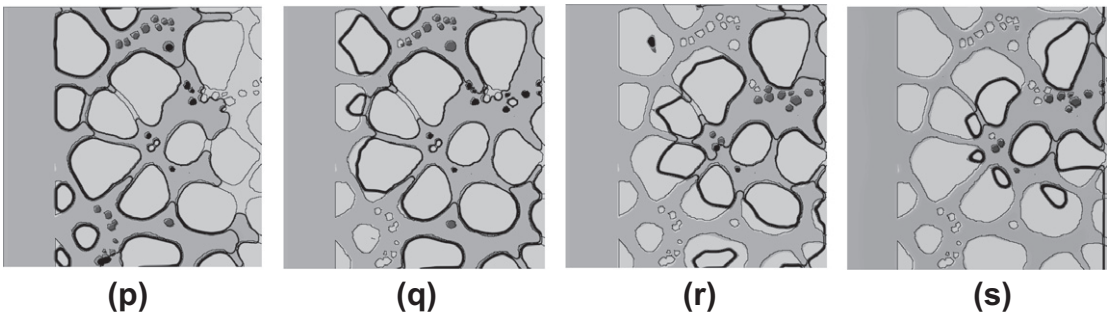

Fig 9. *(continued)*

reduced time $t^* = 3$, 6, 9 and 12, while Fig. 9p–s shows the dislocation configurations for $L = 0.01$ at $t^* = 12$, 24, 36 and 48. As one can see from these figures, the reordering kinetics seem to have a profound impact on the γ' shearing process. If reordering is instantaneous (e.g. in the case of $L = 10$), because of the small SESF energy, dislocations shear through both phases almost indistinguishably. When the reordering process is much slower as compared to the shearing process (e.g. in the case of $L = 0.01$), the shearing process is controlled by the reordering kinetics. Even though the dislocations eventually shear through the two-phase microstructure, leading to the same amount of plastic deformation as the instantaneous reordering case ($L = 10$), the strain rate is much smaller. This tends to agree with the experimental observations [30] where dislocations show features of viscous motion at intermediate temperatures. As experimental measurements have indicated that the creep activation energy Q for a Ni-base disk alloy is about 240 kJ mol^{-1} [62], the reordering mobility L in our simulation can be directly linked to temperature by $L = L_0 \exp(-Q/RT)$. Assuming $L = 0.01$ corresponds to 600 °C, the lower bound of the temperature range within which reordering plays a role during deformation, then $L = 0.1$ corresponds to 665 °C, $L = 1$ corresponds to 741 °C and $L = 10$ corresponds to 830 °C.

Fig. 10 shows the amount of plastic strain under 1000 MPa applied shear stress as a function of the reduced time for different values of the reordering kinetic coefficient, L. The slopes of the curves are the strain rates. The upper bound $\left(\varepsilon^p = \frac{Ab}{V} = 0.0039\right)$ is the plastic strain generated by the two partials completely shearing through the {1 1 1} plane cross-section having an area of A, where V is the volume of the crystal (simulation cell). When no reordering is allowed, the maximum plastic strain is 0.002, which corresponds to Fig. 9c ($t^* = 18$): dislocations entered only the relatively wide channels. In reality, $L = 0$ corresponds to athermal shearing (i.e. at low temperatures). When reordering is enabled, however, the plastic deformation exhibits viscous behavior which is common in creep. It can be observed in Fig. 10, for $L = 10$ (open squares, $T = 830$ °C) and $L = 1$ (open triangles, $T = 741$ °C), that the strain rate before $t^* = 10$ is fairly similar, indicating that when the reordering rate is greater than a certain value, or above a certain temperature ($L = 1$, $T = 741$ °C), the process can be deemed essentially instantaneous. The bend-over of the curves is due to the limited simulation cell size; otherwise, a more or less constant shearing rate would be maintained. For $L = 0.1$ (the cross symbols, $T = 665$ °C), the strain rate becomes smaller as further shearing by the dislocations requires reordering. For $L = 0.01$ (open diamonds, $T = 600$ °C), the initial plastic strain rate coincides with the athermal shearing curve (solid circles). Later, as reordering takes place, the strain gradually increases. Undulation of the strain rate differentiates this case from the others as the rate-limiting process is the reordering for small L values. When the reordering process is much slower than dislocation motion, dislocations will first loop around γ' particles; thus they appear to take on more convoluted shapes (Fig. 9l–s) as compared to cases when reordering happens faster (Fig. 9d–k). After the reordering has aided the dislocations to shear through a number of particles, the strain rate increases as the dislocations are able to move further into the γ phase which was previously inaccessible (blocked by γ' particles prior to the SESF shearing process). The dislocations then proceed to loop around the next set of γ' particles that are encountered, followed by a slow reorder-mediated SESF shearing process, resulting in undulation in the strain rate found at $L = 0.01$.

4. Discussion

4.1. Effect of γ/γ' size and shape (local curvature) on critical shear stress

From Fig. 8, it can be observed that small γ' particles are sheared by SESF when reordering is allowed. However, dislocations can only loop around big particles (indicated by solid and dotted circles in Fig. 8b and c) even though reordering is almost instantaneous when $L = 10$. This is because only when the second dislocation begins to shear the precipitate (creating a pseudo-twin)

Author's personal copy

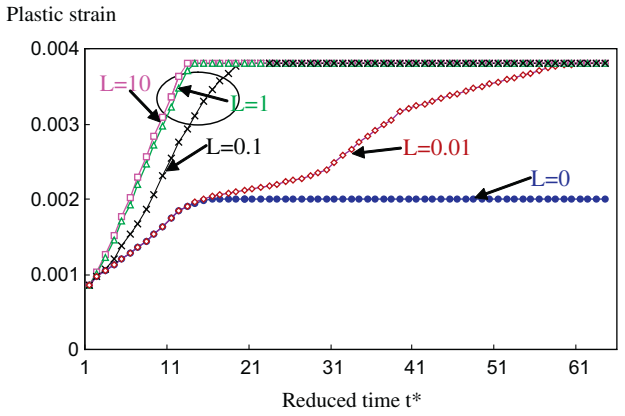

Fig. 10. Plastic strain as function of time under 1000 MPa applied shear stress with different reordering kinetic coefficients L (square: $L = 10$; triangle: $L = 1$; cross: $L = 0.1$; diamond: $L = 0.01$; dot: $L = 0$).

can the reordering process take place and lead to the formation of SESFs. As there is an elastic repulsion between the two partial dislocations, the first partial needs to cut deeply enough into the particle (initially creating a CSF) in order to allow the second one subsequently to enter the particle (as schematically shown in Fig. 11, where r is the γ' particle radius, the solid loop represents the first dislocation that creates CSF in γ' and the dotted loop is the second dislocation that creates SESF when it enters the γ'; their separation distance, H, depends on their elastic interaction and the CSF energy). Assisted by the dislocation line tension, the first partial can cut deeper into smaller particles, thus the critical stress for the SESF shearing becomes a function of the particle radius. Using the dislocation line tension model $T = \frac{\mu b^2}{2}$ in combination with the elastic interaction energy calculation for Volterra-type dislocations, this relation between particle radius

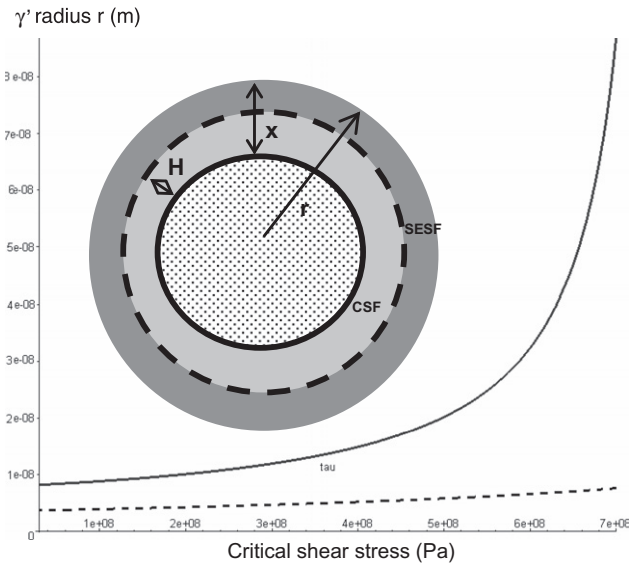

Fig. 11. Relation between critical shear stresses (SESF shearing and CSF shearing) and γ' particle radius.

r and stress τ is shown in Fig. 11 by the solid curve, which is calculated using the material parameters listed in Table 1. The dashed line is the critical shear stress for the leading partial to shear the particle and create a CSF. Under a given applied shear stress, those particles whose sizes are below the solid curve will be sheared by SESFs when reordering is allowed. This calculation also indicates that the CSF energy plays an important role in determining the critical stress for SESF shearing, as higher CSF energy will prevent the first dislocation from cutting deep into the γ' particle and thus prevent the second dislocation from subsequently entering the γ' particle and initiating SESF shearing via reordering.

4.2. Influence of spatial arrangement of γ' particles and γ-channel width on the critical shear stress

Not only does the shape (local curvature) of γ' precipitates influence the critical stress for SESF shearing, but the spatial arrangement of the particles (i.e. the γ-channel width between neighboring γ' particles) plays a critical role as well. One interesting example can be seen in Fig. 8c indicated by the solid white circle. The radius of the particle is about 16 nm. According to Fig. 11, under 500 MPa shear stress the dislocations should be able to shear though and create an SESF because the critical radius is about 20 nm. However, because the trailing dislocation is not able to pass through the γ channels, it is unable to take full advantage of the curvature of the small particle by looping it around together with the leading dislocation. Thus, depending on the channel width, this particle effectively behaves like a γ' particle with larger sizes and cannot be sheared by SESF under 500 MPa.

Fig. 12 shows the phase-field simulation results for several scenarios that the system may experience during shearing (instantaneous reordering with $L = 10$ is used for these simulations and the dislocations are moving from left to right under 600 MPa resolved stress). If there is a large secondary spherical particle (Fig. 12a), just as predicted from Fig. 11, an SESF will not be created even though reordering is enabled. Hence both dislocations loop around the particle. One can also observe that the second dislocation is not even in contact with the γ' particle because of its elastic repulsion with the first dislocation. However, as shown in Fig. 12b, when the secondary particle has a corner with a large local curvature, SESF shearing can still take place. The effect of spatial arrangement is illustrated in Fig. 12c and d, where the only difference between the two cases is that the γ-channel width in (c) is smaller than that in (d). The dislocations are able to sample the high curvature of the individual particles in (d) but not in (c), because the leading dislocation is not able to pass through the γ channel between the particles in the first place. For the same reason, the small tertiary particles shown in Fig. 12f can be sheared individually by SESF, but their cluster as shown in Fig. 12e cannot.

Author's personal copy

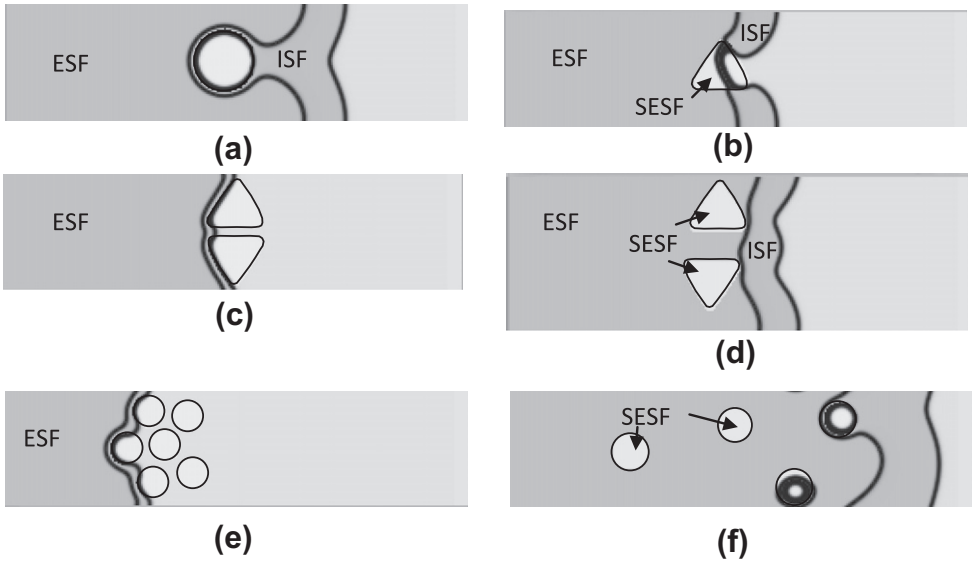

Fig. 12. Effect of particle shape and spatial arrangement on dislocation-precipitate interactions.

4.3. Influence of γ–γ' interface thickness on the critical stress

Recent experimental measurements of composition variation across γ–γ' interfaces using atom probe [63,64] and electron energy loss spectroscopy in a probe-corrected scanning transmission electron microscop [65,66] indicate that the interface width can be up to 4 nm for some γ' particles. In order to investigate how the critical shear stress varies if the GSF energy changes gradually from γ matrix to γ' precipitate across the interface, a simple energy-based calculation is performed for two parallel, straight, pure edge type dislocations interacting with a planar γ–γ' interface as illustrated in Fig. 13. With the interface position located in the middle, the three profiles denote different diffusiveness of the interface, which is represented by a gradual increase in the fault energy. In the matrix, the leading dislocation creates an ISF. When it starts to cut into the γ' phase, it creates a CSF and the energy penalty rises depending on the diffusiveness of the interface which is interpolated between the ISF energy and the CSF energy using a smooth hyperbolic tangent equation:

$$E(x) = (\Gamma^{CSF} - \Gamma^{ISF})\left[\tanh\left(\frac{x}{4t}\right) + 1\right]\Big/2 + \gamma^{ISF} \tag{13}$$

As the value of t increases, the interface width increases and becomes more diffuse (from Fig. 13, it can be seen that the interface width is about t). When the trailing partial shears though on the adjacent {1 1 1} plane, immediate atomic reordering is assumed, so the pseudo-twin structure will instantaneously transform into the low-energy SESF. The position of the leading dislocation is located at $x2$ and that of the trailing one is located at $x1$. The force on the leading dislocation due to the resolved applied shear stress τb and the repulsive force exerted by the trailing dislocation is:

$$f = \frac{\mu b \cdot b(x2 - x1)[(x2 - x1)^2 - d^2]}{2\pi(1 - \nu)[(x2 - x1)^2 + d^2]^2} \tag{14}$$

where $d = 0.207$ nm is the interplanar spacing. The impeding force from creating additional crystal energy as it cuts through the interface is represented by $E(x2)$ (shown in Fig. 13). The trailing partial is under the influence of the applied shear stress τb, the repulsive force from the leading dislocation, f, and the force for reducing CSF energy to SESF energy, $E(x1)$. The equilibrium separation distance of the two dislocations, $(x2 - x1) \approx \frac{\mu b \cdot b}{2\pi(1-\nu)(\Gamma^{CSF} - \Gamma^{SESF})}$, is about 1.9 nm. Thus, the two dislocations move according to the forces they experience, i.e. $\tau b + f - E(x2)$ for the leading partial and $\tau b - f + E(x1)$ for the trailing partial. The interaction between the two is characterized by the repulsive force f. The critical stress for the whole structure to cut into γ' is then obtained by gradually increasing the

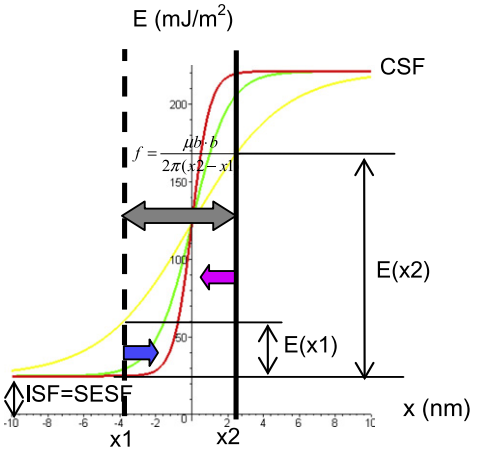

Fig. 13. Influence of γ–γ' interface width on critical SESF shearing stress. Red: boundary width $t = 4$ nm; green: $t = 8$ nm; yellow: boundary width $t = 17$ nm; solid line: position of the leading dislocation; dashed line: position of the trailing dislocation (which is one atomic layer above the leading dislocation glide plane).

Author's personal copy

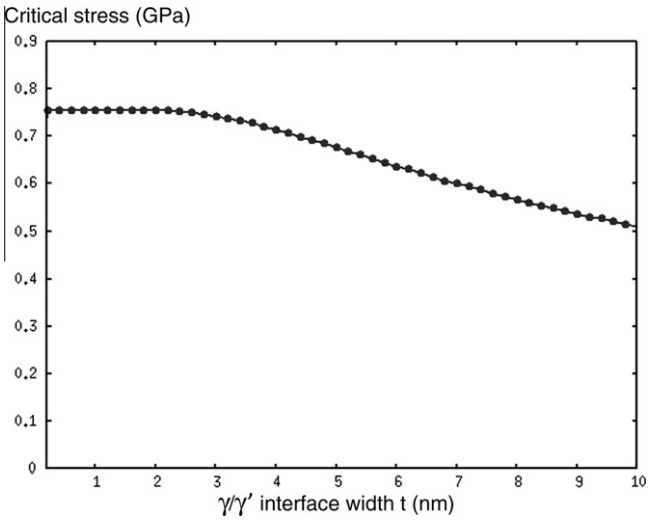

Fig. 14. Critical stress for SESF shearing as a function of interface width.

applied stress. The relationship between the interface width and the critical shear stress is plotted in Fig. 14.

From Fig. 14, it can be seen that the critical stress decreases with increasing interface width. The critical stress for the sharp interface case is given by the planar interface limit: $\frac{\Gamma^{CSF}}{2b} = 756.8$ MPa. As mentioned in Section 4.1, the magnitude of the CSF energy is important because it directly influences the critical stress for the activation of the SESF shearing. Since the interface width can actually be as large as 4 nm for secondary γ' particles [60], the critical stress can be reduced from the sharp interface limit of 757 MPa down to about 710 MPa (for $t \approx 4$ nm). This is, however, a rather insignificant effect as compared to those due to local curvature and the spatial arrangement of γ' particles discussed above. A diffuse dislocation core will have a similar effect as a diffuse γ–γ' interface since it makes the GSF transition smoother. According to the Peierls model [67], for a interplanar spacing of $d = 0.207$ nm and Poisson ratio of $v = 0.4$, the core width of an edge dislocation is about $w = \frac{d}{1-v} = 0.345$ nm and that of a screw dislocation is about $w = d = 0.207$ nm. Comparing these values to the width of the interface, the core size effect on the critical SESF shearing stress can be safely ignored.

4.4. Effect of reordering kinetics and dislocation mobility

In order for the SESF shearing mechanism to operate, a critical stress needs to be reached for a given microstructure. From previous discussions, it can be deduced that higher stress is required for systems with higher CSF energy or larger precipitate size. If the stress level is achieved for most γ' particles, the reordering process should then be rate limiting under intermediate temperature, and therefore control the creep process [30]. As Fig. 9l–s shows, the motion of the dislocations is limited by the formation of SESFs through reordering inside the γ' precipitates.

Indeed, it is actually the ratio of the ordering mobility and the dislocation mobility, L/M_η, that determines the SESF shearing behavior. As a material parameter, the dislocation mobility M_η is expected to be less sensitive to temperature within the temperature range of interest since the dislocations are moving on close-packed planes and do not appear to dissociate in a non-planar configuration [1]. On the other hand, L is a strong function of temperature since it is directly linked to the diffusion-mediated reordering process in the γ' phase.

4.5. Effect of lattice misfit

As mentioned earlier, the lattice misfit of a disk alloy is usually small. However, ongoing research efforts tend to increase the lattice misfit at the rim region of a turbine disk to improve its creep resistance. To investigate how the SESF shearing process is impacted by a larger lattice misfit, e.g. close to the values typically existing in a blade superalloy, a 3-D phase-field simulation cell (edge length 426 nm) is used to obtain the equilibrium shape of a γ' particle with an interfacial energy of 50.2 mJ m^{-2} [5]. A periodic boundary condition is used and the volume fraction of the γ' is 30%. The lattice misfit between the precipitate and the matrix is selected to be $\frac{2(\alpha^{\gamma'}-\alpha^{\gamma})}{(\alpha^{\gamma'}+\alpha^{\gamma})} = 0.24\%$, which makes the

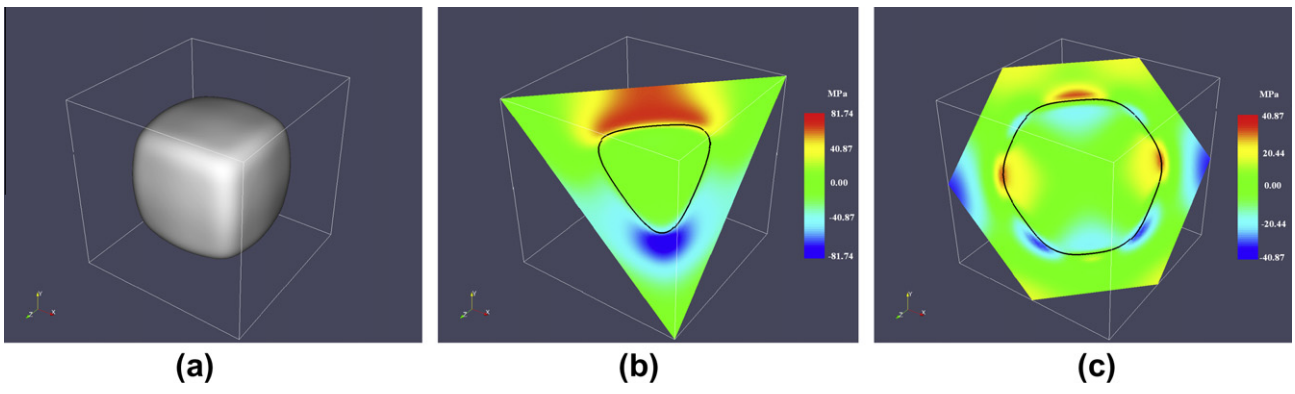

Fig. 15. (a) The equilibrium shape of a γ' particle embedded in γ matrix with a lattice misfit of 0.24%. (b and c) The elastic interaction contour between misfit stress and partial dislocation on different (1 1 1) planes.

Author's personal copy

equilibrium shape of the particles appear cuboidal as shown in Fig. 15a. The same cubic elastic constants are used for both γ and γ' phase: $C_{11} = 224.3$ GPa, $C_{12} = 148.6$ GPa, $C_{44} = 125.8$ GPa [61].

The elastic interaction energy between the microstructure and a $a/6[1\bar{2}1](1\,1\,1)$ partial dislocation can be written as:

$$I = -\sigma_{ij}^{misfit} \cdot \varepsilon_{ij}^{\alpha^*} \tag{15}$$

where σ_{ij}^{misfit} is the misfit stress created by the coherent γ' particle and $\varepsilon_{ij}^{\alpha^*} = \frac{(b_i^\alpha m_j^\alpha + m_i^\alpha b_j^\alpha)}{2d}$ is the eigenstrain of the partial dislocation (see Eq. (9)). The interaction energy contour can be plotted on different (1 1 1) slip planes as illustrated in Fig. 15b and c with the γ–γ' interfaces outlined by black lines. Positive interaction energy means that the misfit stress assists dislocation shearing, while negative value means the opposite. With an interplanar spacing of $d = \frac{a}{\sqrt{3}}$ (where a is the lattice constant) and a Burgers vector of $|b| = \frac{a}{\sqrt{6}}$, the resolved shear stress on this $a/6[1\bar{2}1](1\,1\,1)$ dislocation coming from the misfit stress is: $\tau^{RSS} = \frac{I}{|\mathbf{b}|/d} = -\sqrt{2}\sigma_{ij}^{misfit} \cdot \frac{(b_i^\alpha m_j^\alpha + m_i^\alpha b_j^\alpha)}{2d}$. Thus, this effect is basically $\sqrt{2}$ times the elastic interaction. From the analysis in the first section of the discussion, if the leading $a/6\langle 1\,1\,2\rangle$ dislocation can overcome the CSF energy and cut deeper into γ', then it is easier for the trailing particle to cut into γ' and form an SESF. However, from Fig. 15b and c, the positive interaction energy (resolved shear stress) does not penetrate far into the precipitate and the magnitude of the resolved shear stress is relatively small (lower than 60 MPa even for this large γ' particle with an edge length of about 290 nm). Thus, it appears that the misfit stress effect will be modest.

The other effect arising from the lattice misfit is the equilibrium precipitate shape [68–71]. As the misfit increases, the equilibrium shape of a γ' precipitate will change from a more spherical to a more cuboidal shape (Fig. 15a). The cross-section of a cuboidal γ' will have either a triangular shape (Fig. 15b) or a hexagonal shape (Fig. 15c). The triangular shape has acute angle corners that will serve as preferred locations for initiating SESF shearing, as discussed in Section 4.1. The change of equilibrium γ' particle shape due to misfit will therefore have a larger impact on the SESF shear process than the resolved misfit stress itself.

5. Conclusion

A new GSF energy surface incorporating a diffusion degree of freedom is created to describe the concurrent dislocation shearing and atomic reordering taking place at intermediate temperatures in Ni-base disk alloys. Based on this energy surface, the interaction between dislocation and γ–γ' microstructure is simulated using the phase-field method. Parametric study of the reordering kinetics is carried out to demonstrate the influence of short-range diffusion in the γ' phase on the plastic deformation. Effects of precipitate microstructure and fault energies on the CRSS for SESF shearing are also investigated.

An important finding of this study is that the critical stress for SESF shearing is linearly related to the CSF energy, Γ^{CSF}. Thus, Γ^{CSF} is the dominant material parameter in determining whether or not SESF shearing can operate. Increasing the CSF energy can most effectively inhibit the activation of this reordering-assisted shearing mechanism.

The critical stress is also sensitive to the size and shape of the γ' particle cross-section on the slip plane (the interface curvature) and the spatial arrangement of those particles. In order to avoid the formation of microtwins through SESF shearing of γ' at intermediate temperatures, which lowers the strain-hardening rate, large spherical γ' particles are desired, which means that the lattice misfit between the precipitate and matrix should be kept small. Narrow γ channels between γ' particles and clustering of smaller γ' precipitates can also effectively increase the resistance to SESF shearing. The effect of the γ/γ' interface width and dislocation core width on the critical SESF shearing stress is relatively small.

The simulation results also indicate that, when the critical stress for SESF shearing is achieved for a given microstructure, the strain rate of SESF shearing is sensitive to temperature. As reordering (a short-range diffusion process in the γ' phase) is a much slower process as compared to dislocation glide even at intermediate temperatures (600–800 °C) and relatively high stress level (500–1000 MPa), dislocation motion will clearly exhibit viscous behavior which appears to be dragged by the SESF behind it.

Acknowledgements

We gratefully acknowledge many helpful discussions with Dr. Libor Kovarik and Dr. Ray Unocic. This work is supported by Air Force Research Laboratories through the Metals Affordability Initiative (MAI) Durable Disk program and by GE Aviation through the University Strategic Alliance program (N.Z., M.J.M. and Y.W.), Air Force Office of Scientific Research under Grant No. FA9550-09-1-0014 (Y.W. and M.J.M.), NSF under Grant No. CMMI-0728069 (J.L. and Y.W.), and NSF under Grant No. DMR-1008104, ONR under Grant No. N00014-05-1-0504, and AFOSR Grant No. FA9550-08-1-0325 (J.L.). Most of the simulations were performed at the Arctic Region Supercomputing Center.

References

[1] Kovarik L, Unocic RR, Li J, Sarosi P, Shen C, Wang Y, et al. Prog Mater Sci 2009;54:839.
[2] Pollock TM, Argon AS. Acta Metall Mater 1992;40:1.
[3] Pollock TM, Argon AS. Acta Metall Mater 1994;42:1859.
[4] Fahrmann M, Hermann W, Fahrmann E, Boegli A, Pollock TM, Sockel HG. Mater Sci Eng A 1999;260:212.
[5] Zhou N, Shen C, Mills MJ, Wang Y. Acta Mater 2007;55:5369.

Author's personal copy

[6] Zhou N, Shen C, Mills MJ, Wang Y. Acta Mater 2008;56:6156.
[7] Zhou N, Shen C, Li J, Mills MJ, Wang Y. Development of microstructure-and mechanism-based modeling tools for plastic deformation in multiphase alloys. In: Advances in heterogeneous material mechanics 2008. Lancaster: Destech Publications Inc.; 2008. p. 432–2.
[8] Zhou N, Shen C, Sarosi PM, Mills MJ, Pollock T, Wang Y. Mater Sci Technol 2009;25:205.
[9] Zhou N, Shen C, Mills M, Wang YZ. Philos Mag 2010;90:405.
[10] Gaubert A, Le Bouar Y, Finel A. Philos Mag 2010;90:375.
[11] Gaubert A, Finel A, Le Bouar Y, Boussinot G. Viscoplastic phase field modelling of rafting in Ni base superalloys. Continuum models and discrete systems CMDS 11; 2007.
[12] Reed RC. The superalloys—fundamentals and applications. New York: Cambridge University Press; 2006.
[13] Unocic RR, Viswanathan GB, Sarosi PM, Karthikeyan S, Li J, Mills MJ. Mater Sci Eng A 2008;483:25.
[14] Unocic RR, Kovarik L, Shen C, Sarosi PM, Wang Y, Li J, Ghosh S, Mills MJ. Deformation mechanisms in Ni-base disk superalloys at higher temperatures. In: Superalloys 2008. Warrendale (PA): Minerals Metals & Materials Society; 2008. p. 377–85.
[15] Viswanathan GB, Karthikeyan S, Sarosi PM, Unocic RR, Mills MJ. Philos Mag 2006;86:4823.
[16] Kovarik L, Unocic RR, Li J, Mills MJ. JOM 2009;61:42.
[17] Unocic RR, Kovarik L, Sarosi PM, Shen C, Wang Y, Mills MJ. On the formation and evolution of microtwins during creep deformation in Ni-Base superalloys. In: TMS annual meeting; 2008.
[18] Gleiter H, Hornboge E. Phys Stat Solidi 1965;12:251.
[19] Gleiter H, Hornboge E. Mater Sci Eng 1968;2:285.
[20] Sun YQ, Hazzledine PM. Philos Mag A – Phys Condens Matter Struct Defect Mech Prop 1988;58:603.
[21] Manonukul A, Dunne FPE, Knowles D. Acta Mater 2002;50:2917.
[22] Decamps B, Raujol S, Coujou A, Pettinari-Sturmel F, Clement N, Locq D, et al. Philos Mag 2004;84:91.
[23] Chen QZ, Knowles DM. Mater Sci Eng A 2003;356:352.
[24] Milligan WW, Antolovich SD. Metall Trans A 1991;22:2309.
[25] Viswanathan GB, Sarosi PM, Henry MF, Whitis DD, Milligan WW, Mills MJ. Acta Mater 2005;53:3041.
[26] Kear BH, Oblak JM. J Phys 1974;12:c7.
[27] Kear BH, Oblak JM, Giamei AF. Metall Trans 1970;1:2477.
[28] Vorontsov VA, Shen C, Wang Y, Dye D, Rae CMF. Acta Mater 2010;58:4110.
[29] Foreman AJE, Makin MJ. Philos Mag 1966;14:911.
[30] Kolbe M. Mater Sci Eng A 2001;319:383.
[31] Wang Y, Banerjee D, Su CC, Khachaturyan AG. Acta Mater 1998;46:2983.
[32] Wang YZ, Li J. Acta Mater 2010;58:1212.
[33] Shen C, Li J, Mills M, Wang Y. Modeling shearing of gamma prime in Ni-based superalloys. In: Gottstein G, editor. Integral materials modeling: towards physics-based through-process models. Weinheim: WILEY-VCH Verlag GmbH & Co. KGaA; 2007. p. 243–52. ISBN: 978-3-527-31711-0.
[34] Shen C, Wang Y. Acta Mater 2004;52:683.
[35] Vitek V. Philos Mag 1968;18:773.
[36] Wang Y, Khachaturyan A. Philos Mag A 1995;72:1161.
[37] Veyssiere P, Douin J, Beauchamp P. Philos Mag A 1985;51:469.
[38] Young WM, Elcock EW. Proc Phys Soc Lond 1966;89:735.
[39] Voter AF, Montalenti F, Germann TC. Ann Rev Mater Res 2002;32:321.
[40] Pettinari F, Douin J, Saada G, Caron P, Coujou A, Clement N. Mater Sci Eng A 2002;325:511.
[41] Wang YU, Jin YM, Cuitino AM, Khachaturyan AG. Acta Mater 2001;49:1847.
[42] Frost H, Ashby MF. Deformation-mechanism maps: the plasticity and creep of metals and ceramics. Oxford: Pergamon Press; 1982.
[43] Nabarro FRN. Lond: The Phys Soc 1948:75.
[44] Herring C. J Appl Phys 1950;21:437.
[45] Coble RL. J Appl Phys 1963;34:1679.
[46] Weertman J. J Appl Phys 1955;26:1213.
[47] Asaro RJ, Tiller WA. Metall Trans 1972;3:1789.
[48] Grinfeld MA. Doklady Akademii Nauk Sssr 1986;290:1358.
[49] Cottrell AH, Jaswon MA. Proc Roy Soc Lond Ser A, Math Phys Sci 1949;199:104.
[50] Khachaturyan AG. Sov Phys – Solid State 1967;8:2163.
[51] Khachaturyan AG, Shatalov GA. Sov Phys – Solid State 1969;11:118.
[52] Khachaturyan AG. Theory of structural transformations in solids. New York: Wiley-Interscience; 1983.
[53] Shen C, Wang Y. Acta Mater 2003;51:2595.
[54] Kim SG, Kim WT, Suzuki T. Phys Rev E 1999;60:7186.
[55] Steinbach I, Pezzolla F. Physica D 1999;134:385.
[56] Shen C, Chen Q, Wen YH, Simmons JP, Wang Y. Scripta Mater 2004;50:1029.
[57] Shen C, Chen Q, Wen YH, Simmons JP, Wang Y. Scripta Mater 2004;50:1023.
[58] Balluffi RW, Allen SM, Carter WC. Inetics of materials. New York: John Wiley; 2005.
[59] Zhou N, Wang Y. Manuscript in preparation; 2011.
[60] Sarosi PM, Viswanathan GB, Whitis D, Mills MJ. Ultramicroscopy 2005;103:83.
[61] Kayser FX, Stassis C. Phys Status Solidi A 1981;64:335.
[62] Deutchman H, Mills M. Private communication; 2010.
[63] Sarosi PM, Miller MK, Isheim D, Mills MJ. Microsc Microanal 2007;13:194.
[64] Amouyal Y, Mao Z, Seidman DN. Acta Mater 2010;58:5898.
[65] Hwang JY, Banerjee R, Tiley J, Srinivasan R, Viswanathan GB, Fraser HL. Metall Mater Trans A – Phys Metall Mater Sci 2009;40A:24.
[66] Srinivasan R, Banerjee R, Hwang JY, Viswanathan GB, Tiley J, Dimiduk DM, et al. Phys Rev Lett 2009;102:086101.
[67] Peierls R. Proc Phys Soc 1940;52:34.
[68] Wang Y, Chen LQ, Khachaturyan AG. Acta Metall Mater 1993;41:279.
[69] Wang YZ, Chen LQ, Khachaturyan AG. Scripta Metall Mater 1991;25:1387.
[70] Sequeira AD, Calderon HA, Kostorz G. Scripta Metall Mater 1994;30:7.
[71] Fahrmann M, Fratzl P, Paris O, Fahrmann E, Johnson WC. Acta Metall Mater 1995;43:1007.